J. Electrochem. Sci. Eng. **16** (2026) 3153; https://doi.org/10.5599/jese.3153

Open Access : : ISSN 1847-9286
https://pub.iapchem.org/ojs/index.php/JESE

Original scientific paper

Polymer-controlled growth of BiSI/$Bi_{13}S_{18}I_2$ thin films for photoelectrochemical applications

Xeniya Leontyeva ✉, Gulinur Khussurova and Darya Puzikova

D.V. Sokolsky Institute of Fuel, Catalysis and Electrochemistry JSC, Almaty, Kazakhstan

Corresponding Author: ✉leontyeva.xeniya@mail.ru

Received: November 5, 2025; Accepted: February 10, 2026; Published: February 23, 2026

Abstract

This study investigates, for the first time, the influence of polyvinylpyrrolidone (PVP) concentration in the precursor solution on the structural, morphological, and photoelectrochemical (PEC) properties of BiSI/$Bi_{13}S_{18}I_2$ thin films synthesized via one-step chemical bath deposition. By varying the PVP content from 0 to 3.0 wt.%, a clear correlation is established between polymer-assisted precursor stabilization, phase formation pathways, and the resulting PEC performance. SEM and XRD analyses reveal that 2.5 wt.% PVP yields dense, uniform, and highly crystalline heterophase BiSI/$Bi_{13}S_{18}I_2$ films with minimized grain-boundary density, whereas insufficient polymer leads to discontinuous coatings and excess PVP induces surface passivation and suppressed crystallization. The optimized film (2.5 wt.% PVP) exhibits the highest photocurrent density (15.7 ± 0.31 μA cm^{-2}) and quantum efficiency (IPCE at 465 nm = 2.62 ± 0.04 %) in 0.5 M Na_2SO_4. To elucidate interfacial charge-transfer kinetics and operational stability, the PEC behaviour was further investigated in electrolytes with varying redox activity: Na_2SO_4, Na_2SO_3, and a mixed electrolyte of Na_2SO_3 + Na_2SO_4. The inert sulphate electrolyte reflects intrinsic semiconductor performance and provides the highest stability, whereas sulphite-containing solutions reveal defect-mediated pathways, accelerated hole extraction, and increased susceptibility to photocorrosion. The mixed electrolyte yields the highest photocurrent (25.21 ± 0.38 μA cm^{-2}) but also demonstrates amplified dark currents and gradual degradation. These results establish a structure-property-performance relationship for Bi-based chalcohalide photoanodes and provide practical guidelines for tuning polymer concentration and electrolyte composition to enhance PEC efficiency and stability in aqueous solar-driven systems.

Keywords

Chalcohalide semiconductors; polymer-mediated growth; photoelectrochemical properties; visible-light photoanodes

Introduction

Efficient conversion of solar energy into electrical and chemical forms remains one of the most important tasks in the development of sustainable energy technologies. In photoelectrochemical (PEC) devices, the performance and operational stability of semiconductor electrodes are primarily governed by their electronic structure, defect chemistry, and charge-transfer behaviour at the semiconductor/electrolyte interface [1]. For this reason, the search for safe, low-cost, composition-tolerant, and efficient photoelectrode materials remains a central challenge for PEC systems [2].

A wide range of semiconductors has been investigated as photoelectrodes, including organic materials, metal-organic frameworks, and inorganic compounds [3]. Over the past decade, particular attention has shifted to inorganic oxides and oxynitrides (ZnO, SnO_2, TiO_2, Cu_2O, $CuBi_2O_4$, Fe_2O_3, $BiVO_4$, $BiWO_4$, BiOI, BiOS, WO_3, *etc*.) due to their high PEC stability, low manufacturing cost, and structural tunability [3-11]. Halide perovskites have also emerged as promising solar absorbers [12]. However, their practical implementation is strongly constrained by poor moisture and thermal resistance a, as well ashe presence of toxic lead [13]. These limitations motivate the development of lead-free, environmentally friendly materials with comparable optoelectronic performance.

Bismuth-based semiconductors are currently considered among the most promising candidates due to the defect-tolerant electronic configuration of Bi^{3+} ($6s^26p^3$), low toxicity, high chemical resistance and favourable optoelectronic characteristics [14]. It has recently been demonstrated not only in PEC systems but also in advanced visible-light-driven bismuth-based heterostructured photocatalysts exhibiting high activity and stability in aqueous environments [15]. In particular, bismuth chalcohalides such as BiSI and $Bi_{13}S_{18}I_2$ have attracted increasing attention as visible-light absorbers in PEC applications. The optical properties of these compounds are highly dependent on their crystalline phase. While the orthorhombic BiSI phase exhibits a band gap in the range of 1.5 to 1.8 eV [16,17], the iodine-deficient hexagonal $Bi_{13}S_{18}I_2$ phase (also referred to as $Bi_{19}S_{27}I_3$) possesses a narrower band gap of approximately 0.7 to 1.1 eV [18,19]. Their strong absorption across the visible to near-infrared range, coupled with intrinsic structural anisotropy, provides a framework for efficient charge separation and transport [20]. Photocurrent densities up to 5 mA cm^{-2} under AM 1.5G illumination have already been demonstrated for BiSI-based photoanodes [21], emphasizing the applicability of these materials for regenerative PEC systems and solar-to-chemical energy conversion.

Structurally, BiSI and $Bi_{13}S_{18}I_2$ are distinct bismuth sulphoiodide compounds with different stoichiometry and crystal structures. Orthorhombic BiSI (space group Pnam) consists of one-dimensional double chains of Bi-S-I units, which result in pronounced intrinsic structural and electronic anisotropy [22]. In contrast, hexagonal $Bi_{13}S_{18}I_2$ (space group $P6_3/m$) features a branched three-dimensional anionic framework with a more isotropic connectivity [23].

The intrinsic anisotropy of optical absorption and charge-transport properties originates from the crystallographic arrangement within each individual phase. In heterophase BiSI/$Bi_{13}S_{18}I_2$ thin films, the coexistence of these structurally distinct compounds influences the effective charge-transfer pathways, interfacial transport, and recombination behaviour, rather than being the primary origin of anisotropy itself [24].

Due to these advantages, BiSI is considered one of the most promising photoanode materials for PEC water-splitting systems, regenerative PEC cells, and hybrid solar technologies [25-27], and it also shows potential for ionizing-radiation detection [28].

Thin-film fabrication remains the key factor limiting PEC performance. Chemical bath deposition (CBD) is one of the most attractive approaches for BiSI synthesis due to simplicity, scalability and mild processing conditions [29,30]. It is well known that uncontrolled nucleation and rapid particle

aggregation during solution-based thin-film deposition can result in rough, non-uniform coatings with defect-rich grain boundaries, which in turn degrade charge-separation efficiency and increase interfacial recombination losses [31,32].

The introduction of polymer additives is considered an effective way to regulate crystal nucleation and growth kinetics [33,34]. Polyvinylpyrrolidone (PVP), in particular, is a multifunctional additive commonly used in wet-chemical syntheses to control nucleation density, crystal growth, and film morphology [35-38]. The carbonyl groups of PVP can coordinate Bi^{3+} ions, reducing their free activity in solution and stabilizing solvated metal-ligand complexes [39]. This coordination lowers the rate of homogeneous nucleation while promoting heterogeneous nucleation on the substrate surface, leading to improved film uniformity [40]. In thiourea-containing Bi-S-I precursor systems, polyvinyl-pyrrolidone (PVP) acts as an effective kinetic regulator of nucleation and crystal growth [41]. The carbonyl groups of PVP coordinate Bi^{3+} ions, stabilizing Bi-thiourea complexes and reducing the activity of free metal cations in solution [42]. This coordination moderates the thermal decomposition of thiourea and ensures a controlled release of sulphide species, thereby suppressing uncontrolled homogeneous precipitation of bismuth sulphide phases in the solution bulk. Moreover, selective adsorption of PVP on specific crystallographic facets alters growth anisotropy, influencing particle shape, grain connectivity, and film adhesion to the fluorine-doped tin oxide (FTO) substrate. As a result, optimized PVP concentrations promote the formation of dense, well-connected BiSI/$Bi_{13}S_{18}I_2$ thin films with reduced defect density, thereby improving charge transport, suppressing interfacial recombination, and enhancing photoelectrochemical performance [43,44].

The photoelectrochemical activity of BiSI thin films and nanostructures has been investigated using various synthesis approaches, including solvothermal methods [45], chemical bath deposition [46,47], spray pyrolysis [21,48], spin coating [49], and a low-temperature anion-exchange route [50]. The influence of synthesis parameters on interfacial charge-transfer processes remains a critical challenge for the rational design of efficient photoelectrodes. Recent advances in photo-driven electrochemical systems, including dual-cathode photoelectro-Fenton architectures for water decontamination, have clearly demonstrated that electrolyte composition, interfacial chemistry and controlled charge transport are decisive factors governing both efficiency and long-term stability of photoelectrochemical devices [51].

However, for BiSI-based photoelectrodes, the influence of PVP concentration on the combined physicochemical and PEC characteristics of BiSI, including phase composition, morphology, photocurrent density, IPCE and long-term photocurrent stability, has not yet been systematically investigated. The absence of quantitative correlations between polymer content, microstructure evolution and PEC properties limits the rational design of highly efficient BiSI-based photoelectrodes.

The aim of the present work is to determine how the concentration of PVP in the precursor solution affects the morphology, phase composition and PEC properties of BiSI/$Bi_{13}S_{18}I_2$ thin films obtained by CBD. Special attention is given to establishing quantitative relationships between PVP concentration and PEC performance parameters, including photocurrent density (IPCE) and operational stability. The results enable optimization of synthesis conditions to develop high-performance BiSI photoanodes suitable for use in regenerative PEC systems.

Experimental

Chemicals

All experiments were carried out using analytical-grade reagents and distilled water. Glass plates with an FTO coating (Sigma-Aldrich) were used as substrates. For preliminary cleaning of the FTO substrate surface, a soap solution, ethanol (96 % C_2H_5OH), hydrogen peroxide (50 % H_2O_2) and an

aqueous solution of ammonia (33 % NH_4OH) were used. The precursor solution for chemical bath deposition was prepared by dissolving 0.01 M $Bi(NO_3)_3$ $5H_2O$, 0.1 M thiourea ($CS(NH_2)_2$), 0.015 M KI and the required amount of polyvinylpyrrolidone (PVP, $(C_6H_9NO)_n$, $M_m \approx 360\,000$) in 100 mL of 0.1 M HNO_3 at 45 °C under constant stirring. To investigate the effect of PVP concentration on the physicochemical and photoelectrochemical properties of the BiSI/$Bi_{13}S_{18}I_2$ films, PVP contents of 0, 0.8, 1.6, 2.5, and 3.0 wt.% were used. Aqueous sodium sulphate (0.5 M Na_2SO_4) was used for the preparation of electrolytes for PEC measurements.

Synthesis of BiSI thin films

BiSI/$Bi_{13}S_{18}I_2$ thin films were synthesized on FTO substrates using the CBD method, following an optimized procedure based on earlier work for related systems [43]. The FTO plates were cut into 10×25 mm pieces and subjected to stepwise cleaning: degreasing in ethanol, rinsing in a soap solution, and boiling for 10 min in a mixture of 50 % H_2O_2 and 33 % NH_4OH (1:1 v/v). The substrates were rinsed with distilled water and dried before deposition. Film growth was carried out by fully immersing the prepared FTO substrates in the precursor bath preheated to 65 °C. The deposition time was fixed at 60 min, as determined previously to yield optimal film coverage [44]. After deposition, the substrates were rinsed with distilled water containing a small amount of concentrated HNO_3 to remove loosely bound precipitates and dried at 90 °C for 15 min.

Since BiSI also tends to precipitate homogeneously in the solution bulk, the reaction mixture was filtered immediately before deposition to minimize secondary nucleation and ensure reproducible film morphology.

A schematic summary of the CBD process is provided in Figure 1.

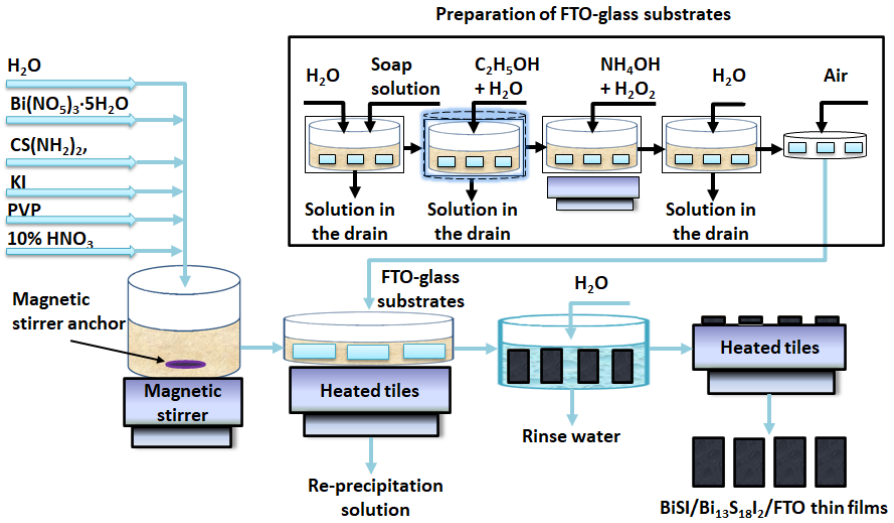

***Figure** 1. Schematic representation of the chemical bath deposition (CBD) process used for the preparation of BiSI thin films*

Physicochemical characterization methods

The surface morphology and particle distribution of the films were examined using a JSM-6610LV scanning electron microscope (JEOL, Japan). The elemental composition was determined by energy-dispersive X-ray spectroscopy (EDX) integrated into the JEOL JSM-6610LV SEM (Oxford Instruments X-Max, 20 mm^2 detector). The phase composition and crystal structure were analysed using a DRON-4-07 X-ray diffractometer ($CoK_{\alpha 1}$ radiation, λ = 0.179 nm, 25 kV, 25 mA). Diffraction patterns were processed using the Match! software package with the COD-Inorg database. Quantitative phase analysis and refinement of structural parameters were carried out by the Rietveld method

using FullProf Suite, including the evaluation of lattice parameters, phase mass fractions and goodness-of-fit indicators (R_p, R_{wp}, R_{exp}, χ^2). The refined crystal lattice parameters were compared with reference data for BiSI (JCPDS 043-0652), $Bi_{13}S_{18}I_2$ (JCPDS 073-1157), and BiOI (JCPDS 10-445).

Photoelectrochemical measurements

Photoelectrochemical (PEC) measurements were carried out in a 30 mL three-electrode cell comprising a BiSI/$Bi_{13}S_{18}I_2$/FTO working electrode, a platinum wire counter electrode and an Ag/AgCl (3 M KCl) reference electrode. All PEC experiments were performed using a Metrohm Autolab PGSTAT302N potentiostat/galvanostat. A blue LED (λ = 465 nm) was used as the irradiation source for PEC measurements. This wavelength was chosen because its photon energy (~2.7 eV) exceeds the band gaps of both orthorhombic BiSI (1.6-1.8 eV) and hexagonal $Bi_{13}S_{18}I_2$ (~0.8-1.1 eV), ensuring strong optical absorption and efficient generation of photoexcited charge carriers in both phases. Such excitation conditions are suitable for comparative analysis of the influence of PVP concentration on the photoelectrochemical behaviour of the BiSI/$Bi_{13}S_{18}I_2$ heterophase films. During measurements, the working electrode was illuminated from the semiconductor side using a blue LED (λ = 465 nm, intensity M Na_2SO_4) in a pulsed regime (5 s light / 5 s dark). The illumination intensity was calibrated before each experiment using a silicon photodiode. Aqueous solutions of 0.5 M Na_2SO_4, 0.1 M Na_2SO_3, and their mixtures were used as electrolytes.

The incident photon-to-current efficiency (IPCE, %) spectra were recorded under monochromatic illumination using a monochromator. IPCE, also referred to as the external quantum efficiency (EQE, %), represents the percentage ratio of the number of photogenerated charge carriers collected by the photoelectrode to the number of photons incident on its surface. The IPCE was calculated according to Equation (1) [52]:

$$\mathrm{IPCE}(\lambda) = \mathrm{EQE} = \frac{J_{ph}(\lambda)1239.8}{P_l(\lambda)\lambda}100 \quad (1)$$

where J_{ph} / mA cm^{-2} is the photocurrent density at a wavelength of incident light (λ / nm), P_l / mW cm^{-2} is the intensity of incident radiation at a wavelength λ.

For a fixed wavelength (*e.g.* λ = 465 nm), the calculated IPCE value corresponds to the external quantum efficiency at this wavelength. The long-term operational stability of the photoelectrodes was assessed by monitoring the photocurrent density over time at a fixed applied potential.

Electrochemical impedance spectroscopy

Electrochemical impedance spectroscopy (EIS) measurements were performed using a Metrohm Autolab PGSTAT302N potentiostat controlled by NOVA software. The measurements were carried out in a three-electrode configuration with the BiSI/$Bi_{13}S_{18}I_2$/FTO electrode as the working electrode (geometric area 1 cm^2), a platinum wire counter electrode, and an Ag/AgCl (3 M KCl) reference electrode. EIS spectra were recorded in 0.5 M Na_2SO_4, 0.1 M Na_2SO_3 and 0.1 M Na_2SO_3 + 0.5 M Na_2SO_4 electrolytes at a fixed applied potential corresponding to the stable photocurrent region. Measurements were conducted under continuous blue LED illumination (λ = 465 nm, 10 mW cm^{-2}) after a stabilization period of 5 min. The impedance spectra were collected over a frequency range from 100 kHz to 0.1 Hz with an AC perturbation amplitude of 10 mV. The experimental data were analyzed by fitting an equivalent circuit model, R_s-(R_{ct}‖CPE), to the impedance spectra using nonlinear least-squares optimization. This approach was used instead of a simple semicircle fit to account for non-ideal interfacial capacitive behavior characteristic of polycrystalline heterophase photoelectrodes.

The constant phase element (CPE) was introduced to describe the non-ideal capacitive response of the semiconductor/electrolyte interface. Its impedance is defined as $Z_{CPE} = 1/[Q(j\omega)^n]$, where Q / Ω^{-1} s^n is the CPE coefficient, n ($0 \le n \le 1$) is the CPE exponent reflecting the deviation from ideal capacitive behavior (n = 1 corresponds to an ideal capacitor), j is the imaginary unit, and ω is the angular frequency.

Statistical analysis

To ensure the reliability of the results, each synthesis and measurement series was performed at least four times (N = 4), where N denotes independently prepared samples synthesized in separate deposition batches under identical conditions. The values reported in the text, figures, and tables represent mean values ± standard deviation (mean ± SD), reflecting both batch-to-batch synthesis variability and instrumental and measurement-related errors.

For photoelectrochemical measurements, including photocurrent-potential (J_{ph}-E) curves, incident photon-to-current efficiency spectra, and chronoamperometric stability tests, measurements were carried out on all four independently prepared samples. For each sample, measurements were performed at multiple positions on the electrode surface to account for possible surface inhomogeneity and local variations in film thickness or morphology. The final reported values were obtained by averaging all measurements across samples and positions.

For labor-intensive and time-dependent experiments - such as Rietveld structure refinement and long-term photocurrent stability measurements - representative samples are presented. This approach does not affect the credibility of the conclusions and enables an accurate evaluation of the intrinsic physicochemical and photoelectrochemical characteristics of the BiSI/$Bi_{13}S_{18}I_2$ films.

Results and discussion

Formation mechanism of BiSI/$Bi_{13}S_{18}I_2$ thin films and role of polyvinylpyrrolidone

Polyvinylpyrrolidone (PVP) is a water-soluble polymer containing polar amide (pyrrolidone) groups capable of both donating and accepting hydrogen bonds. The high polarity of the pyrrolidone ring originates from the carbonyl oxygen and ring nitrogen atoms, which possess lone electron pairs and can act as coordination sites for metal cations (Figure 2a) [53]. As a result, PVP readily forms coordination complexes with Bi^{3+} ions in solution through ion-dipole and donor-acceptor interactions, leading to the formation of stabilized species of the type $[Bi(PVP)_n]^{3+}$ (Figure 2b) [54].

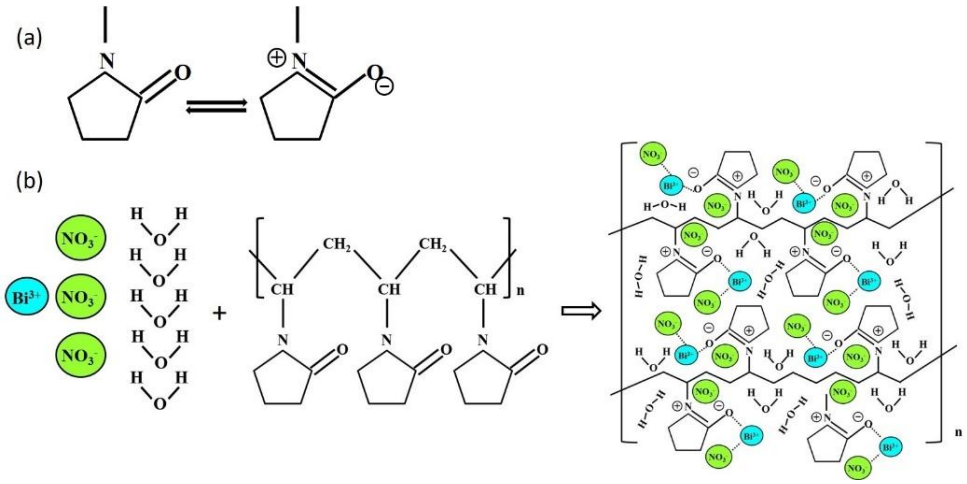

Figure 2. *Coordination mechanism of Bi^{3+} ions by PVP: (a) resonance structure of the pyrrolidone group; (b) formation of $[Bi(PVP)n]^{3+}$ complexes in aqueous solution*

The formation pathway of BiSI/$Bi_{13}S_{18}I_2$ thin films under PVP-controlled conditions, as well as the influence of PVP concentration on film morphology and charge separation behaviour, are schematically illustrated in Figure 3.

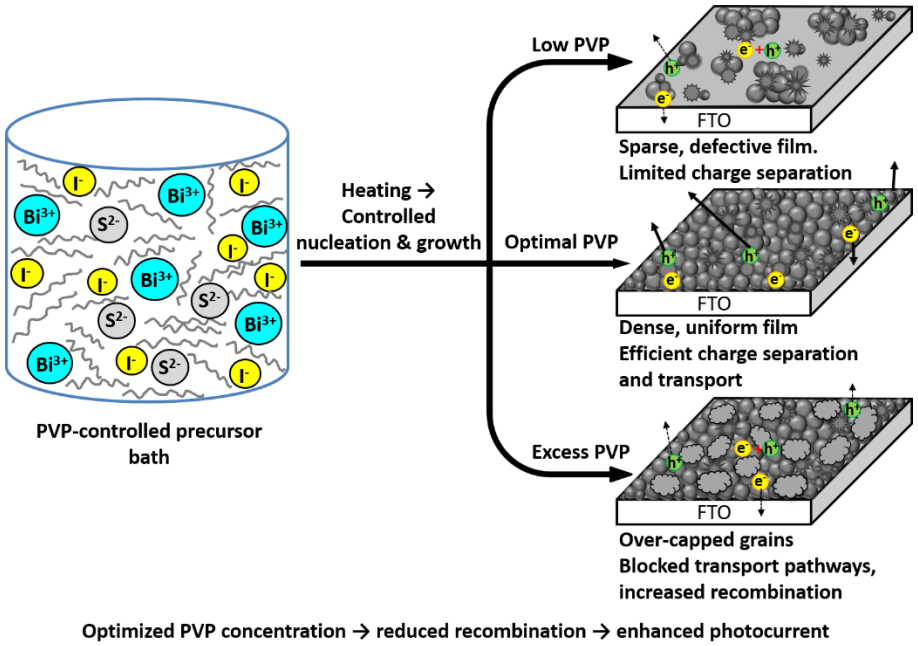

Figure 3. *Schematic illustration of the PVP-controlled nucleation and growth of BiSI/$Bi_{13}S_{18}I_2$ thin films and the resulting impact of PVP concentration on film morphology and charge transport*

Optimal PVP content promotes dense, uniform films with efficient charge transport, whereas insufficient or excessive PVP leads to defective morphology and increased recombination.

In the precursor bath, Bi^{3+} ions are initially coordinated by PVP chains *via* carbonyl groups, forming labile $[Bi(PVP)_n]^{3+}$ complexes. Upon the addition of thiourea, partial ligand exchange occurs and soluble bismuth-thiourea complexes, such as $Bi[CS(NH_2)_2]_2(NO_3)_3$, are formed, while PVP remains in solution as a kinetic and steric stabilizer. In acidic media, thiourea acts as a bidentate ligand coordinating Bi^{3+} ions via sulphur and nitrogen atoms, yielding stable yellow-coloured complexes that remain soluble at room temperature, Equation (2) [55]:

$$Bi(NO_3)_3 + 2CS(NH_2)_2 \rightarrow Bi[CS(NH_2)_2]_2(NO_3)_3 \quad (2)$$

Upon heating, these complexes gradually decompose, releasing sulphide species (S^{2-}), which subsequently react with iodide ions present in the solution. This process results in the nucleation and deposition of BiSI thin films on the FTO substrate, described by Equation (3) [47,56]:

$$Bi[CS(NH_2)_2]_2(NO_3)_2 + KI + 4H_2O + 2HNO_3 \rightarrow BiSI + H_2S + 2CO_2 + 4(NH_4)NO_3 + KNO_3 \quad (3)$$

At elevated thiourea concentrations (*i.e.* increased sulphide availability) and moderate iodide content, combined with partial hydrolysis of Bi^{3+} species, the formation of the hexagonal $Bi_{13}S_{18}I_2$ phase becomes thermodynamically favourable alongside orthorhombic BiSI [20]. This transformation can be described in the ionic approximation by Equation (4):

$$13Bi^{3+} + 18S^{2-} + 2I^- \rightarrow Bi_{13}S_{18}I_2\downarrow \quad (4)$$

The formation of $Bi_{13}S_{18}I_2$ is accompanied by a distinct colour change of the deposit from yellow-orange (BiSI) to dark brown or nearly black, reflecting a reduction in the optical band gap. Crystal growth of $Bi_{13}S_{18}I_2$ preferentially proceeds along the [001] direction, resulting in globular and needle-like aggregates within the thin films.

Beyond complex stabilization, PVP also acts as an effective steric stabilizer during film growth by forming spatial barriers that suppress aggregation of primary nuclei and limit particle coalescence, resulting in more uniform nanostructures with improved adhesion to the FTO substrate [57]. The stabilization mechanism is additionally influenced by hydrogen bonding in the aqueous medium and by hydration shells surrounding metal ions, which together affect complexation equilibria and nucleation kinetics [58]. Furthermore, selective adsorption of PVP on specific crystallographic facets modifies growth anisotropy, influencing particle morphology, grain connectivity, and defect density. Collectively, these effects promote the formation of dense and homogeneous BiSI/$Bi_{13}S_{18}I_2$ thin films with suppressed charge-carrier recombination and enhanced photoelectrochemical performance [59].

Characterizations of BiSI/$Bi_{13}S_{18}I_2$ thin films

Chemical bath deposition produced BiSI/$Bi_{13}S_{18}I_2$ films ranging in colour from yellow-grey (0 wt.% PVP) to dark grey (2.5-3.0 wt.% PVP), reflecting changes in the optical appearance and macroscopic surface coverage with increasing polymer content (Figure 4a). Visual inspection showed that the homogeneity of the coating and the surface texture were strongly dependent on the PVP concentration in the precursor solution. To clarify these effects, a detailed analysis of the film surface morphology was performed.

Figures 4b to 4f show the SEM images of the surfaces of BiSI/$Bi_{13}S_{18}I_2$ thin films synthesized at different PVP concentrations (3.0, 2.5, 1.6, 0.8 and 0 wt.%). The PVP content is found to directly determine the microstructure of the films and the degree of substrate coverage. At 3.0 wt.% PVP (Figure 4b), large globular particles are observed together with smooth, low-contrast regions on the surface, indicating a loss of crystallinity and increased surface heterogeneity at high polymer concentration. Such surface passivation inhibits continuous crystallite growth, resulting in partial exposure of the FTO substrate. At 2.5 wt.% PVP (Figure 4c), a relatively compact surface morphology composed of interconnected globular and star-shaped particles (~0.90 to 1.17 μm) is observed. Almost complete substrate coverage and dense contact between crystallites minimize the number of grain boundaries and form an efficient charge-transfer network. Comparable morphology was reported in [56], where star-shaped $Bi_{13}S_{18}I_2$ structures improved conductivity due to the increased intercrystallite contact area. The observed similarity in microstructural features at the optimal PVP concentration reflects comparable growth conditions rather than a phase-specific morphological signature. A decrease to 1.6 wt.% PVP (Figure 4d) leads to the formation of branched long-needle structures (~1.8 to 2.6 μm), accompanied by reduced film density and numerous interparticle discontinuities. This behaviour indicates insufficient stabilization of precursor complexes and dominant anisotropic growth. At 0.8 wt.% PVP (Figure 4e), predominantly short-needle and partially globular particles are formed, distributed unevenly across the surface. Large uncovered areas of the FTO substrate remain, indicating the absence of a continuous charge-transport pathway. In the absence of PVP, light brown-grey films are produced on the FTO surface, which, according to the SEM micrographs (Figure 4f), consist of highly developed 3D “flower-shaped” microstructures. These aggregates (10-14 μm) are composed of lamellar “petals” 1-2 μm in size, this morphology typically associated with unrestricted axial growth of crystallites, previously reported for BiOI [60]. Between the flower-shaped structures, clusters of “needle-shaped spheres” 1.5-3 μm in diameter are also formed, characteristic of the hexagonal $Bi_{13}S_{18}I_2$ phase [56]. Their simultaneous appearance is attributed to the competing growth of BiOI, BiSI, and $Bi_{13}S_{18}I_2$ in the absence of polymer stabilization; rapid anisotropic growth in multiple crystallographic directions promotes self-assembly into large hierarchical aggregates. The observed flower-like and spheroidal morphologies are consistent with

previous reports on Bi-S-I systems synthesized without stabilizing agents, in which complex hierarchical structures arise from kinetically controlled crystal growth rather than from phase-specific signatures [19,20]. According to phase equilibrium studies of the Bi-S-I ternary system, the coexistence of BiSI with sulphur-richer ternary phases is thermodynamically allowed under non-equilibrium conditions, which may further contribute to morphological diversity [23]. Higher-magnification SEM images (Figure S1, Supplementary material) further confirm the observed morphological trends.

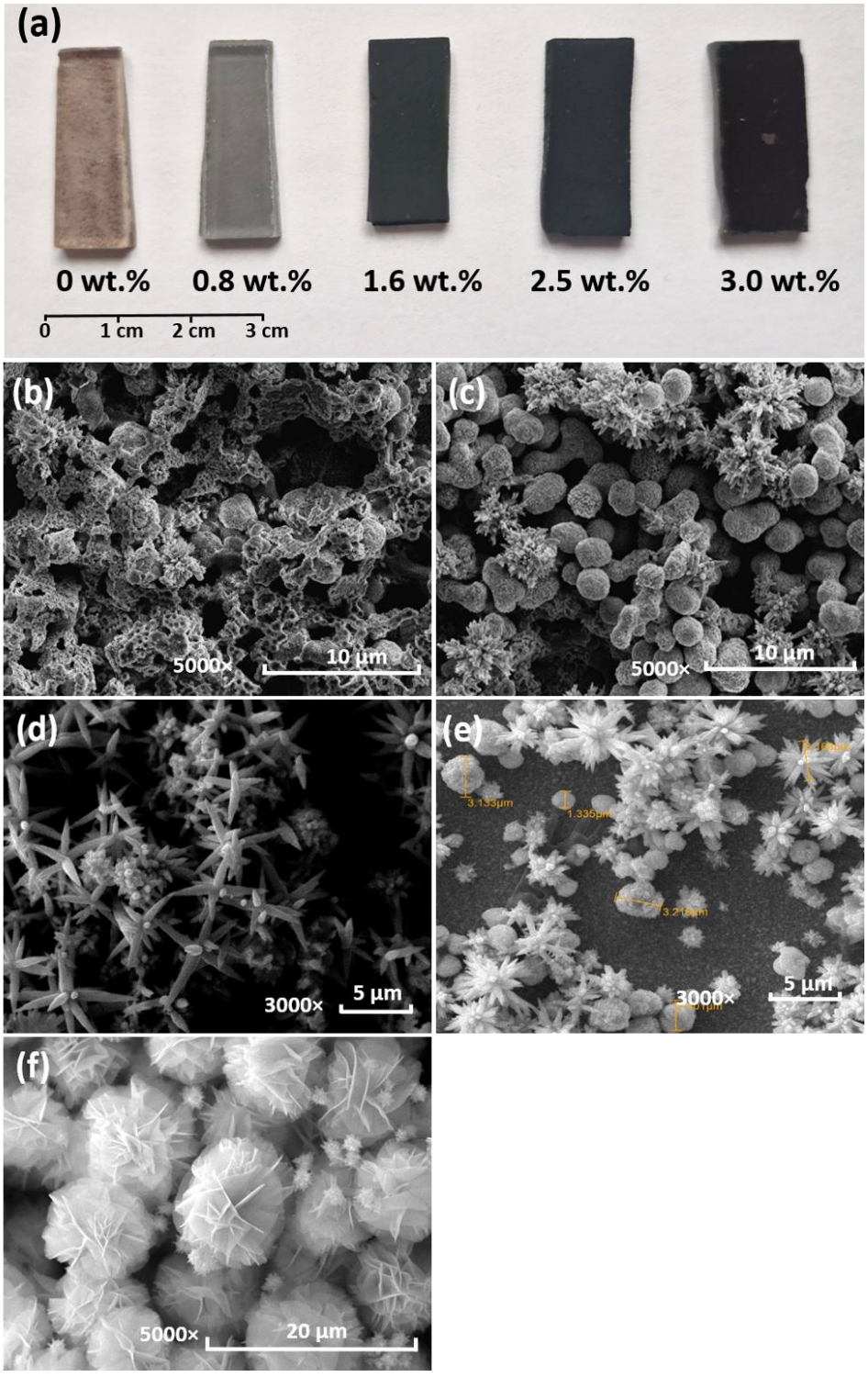

Figure 4. *(a) Photographs of BiSI/ $Bi_{13}S_{18}I_2$ thin films deposited on FTO substrates at different PVP concentrations (0 to 3.0 wt.%), (b-f) SEM images of the surfaces of BiSI/$Bi_{13}S_{18}I_2$ thin films synthesized at different PVP concentrations: (b) 3.0 wt.%; (c) 2.5 wt.%; (d) 1.6 wt.%; (e) 0.8 wt.%; (f) 0 wt.%*

EDS elemental mapping provides qualitative information on the spatial distribution of the elements. As shown in Figure 5, sulphur and iodine exhibit a heterogeneous distribution across the surface. The needle-shaped spherical particles are characterized by a relatively enhanced sulphur signal and a reduced iodine contribution compared to the surrounding flower-shaped matrix. Although EDS mapping does not allow quantitative phase determination, this compositional contrast is consistent with the presence of a sulphur-rich secondary phase, as indicated by XRD analysis.

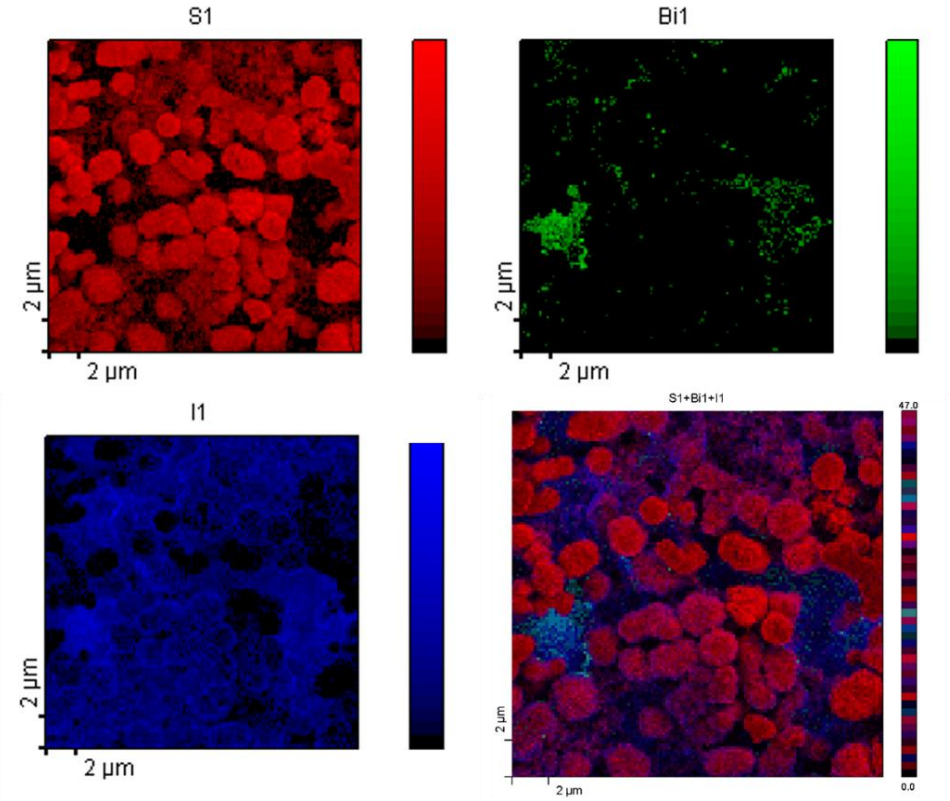

Figure 5. *EDS elemental maps of BiSI/$Bi_{13}S_{18}I_2$ thin film deposited by CBD at a PVP concentration of 2.5 wt.%*

Overall, the morphology analysis indicates that 2.5 wt.% PVP represents the optimal additive concentration, ensuring a balance between stabilizing precursor complexes and promoting directional crystal growth. Excess PVP results in surface passivation and retarded crystallization, whereas insufficient PVP leads to unstable nucleation and discontinuous coatings.

Table 1 presents the averaged EDS elemental ratios of Bi-S-I thin films deposited for 60 min at different PVP concentrations (3.0, 2.5, 1.6, 0.8, and 0 wt.%). These data reflect the overall elemental composition of the films rather than phase-specific contributions. No systematic trend in the Bi:S:I ratios with varying PVP concentration is observed, indicating that the stabilizer primarily affects the growth mode, morphology, and phase distribution rather than the global elemental balance of the films. For samples synthesized at 3.0, 2.5, and 1.6 wt.% PVP, the averaged Bi:S:I ratios remain within the compositional range expected for sulphur-rich Bi-S-I systems. Phase identification for these samples is therefore based exclusively on XRD analysis, which reveals the coexistence of BiSI and $Bi_{13}S_{18}I_2$ phases. At 0.8 wt.% PVP, incomplete and non-uniform substrate coverage is observed (Figure S1g), reflecting the growth mode under the applied deposition conditions. In the absence of PVP (0 wt.%), the film exhibits a pronounced oxygen content and a significant increase in iodine contribution, suggesting partial oxidation and the formation of iodine-rich surface regions. Such deviations may be associated with the formation of a mixed Bi-S-I system dominated by BiSI and

$Bi_{13}S_{18}I_2$ phases, as identified by XRD. In addition, the appearance of plate-like surface features suggests the possible formation of a minor BiOI-related phase.

Table 1. *Overall elemental ratios (Bi:S:I) of Bi-S-I thin films deposited by CBD at different PVP concentrations, determined by EDS*

PVP concentration, wt.%	Content, at.%			
	Bi	S	I	O
3.0	33.62 ± 0.71	58.03 ± 0.31	8.36 ± 0.28	-
2.5	33.34 ± 0.26	56.06 ± 0.28	10.60 ± 0.47	-
1.6	27.95 ± 0.26	35.95 ± 0.26	9.77 ± 0.14	-
0.8	36.83 ± 0.13	51.51 ± 0.42	11.66 ± 0.21	-
0.0	27.28 ± 0.34	12.01 ± 0.41	31.84 ± 0.19	28.88 ± 0.31

Note: EDS data represent averaged surface composition and do not allow phase-specific analysis in multiphase samples

Figure 6 shows the X-ray diffraction patterns of BiSI/$Bi_{13}S_{18}I_2$ thin films synthesized by chemical bath deposition at different PVP concentrations (3.0, 2.5, 1.6, 0.8 and 0 wt.%). Along with reflections from the FTO substrate, the diffraction peaks are assigned to orthorhombic BiSI and hexagonal $Bi_{13}S_{18}I_2$, matching JCPDS 043-0652 and JCPDS 073-1157, respectively, confirming the formation of chalcohalide films on the FTO surface. For the film obtained without PVP (0 wt.%, Figure 6, black line), additional strong reflections of tetragonal BiOI (P_4/nmm, JCPDS 10-445) are detected, while the FTO peaks are absent, indicating the formation of a thick, compact coating. The BiOI peaks located at 29.6, 34.6, 45.4, 54.1, 66.1, 75.1 and 78.6° correspond to the (101), (102), (103), (104), (212), (204) and (214) planes. At 0.8 wt.% PVP (Figure 6, red line), pronounced SiO_2 and SnO_2 reflections appear, demonstrating incomplete substrate coverage.

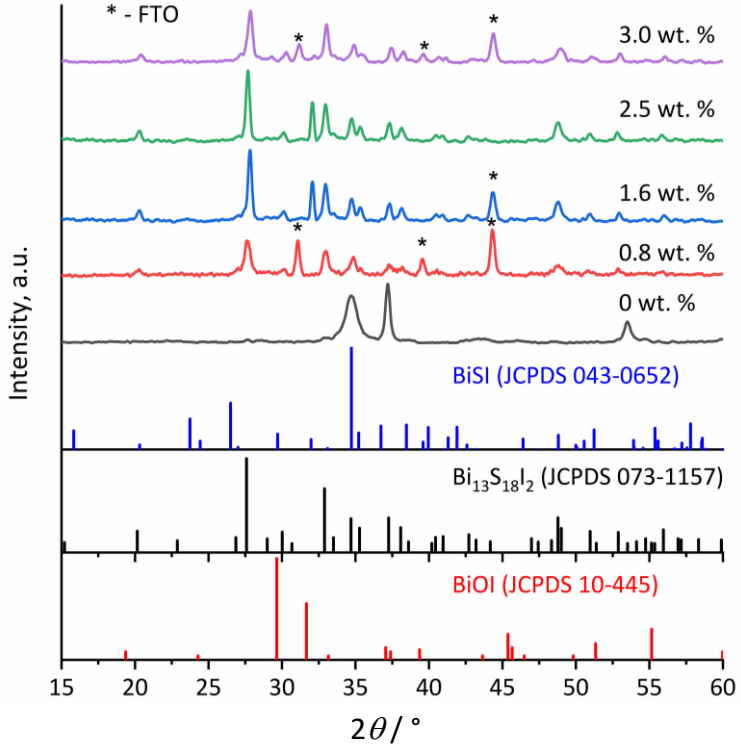

Figure 6. *X-ray diffraction patterns of BiSI/$Bi_{13}S_{18}I_2$ semiconductor thin films deposited via CBD at different PVP concentrations (3.0, 2.5, 1.6, 0.8 and 0 wt.%)*

The intensity of BiSI and $Bi_{13}S_{18}I_2$ peaks is low, which agrees with SEM results. An increase in PVP concentration to 1.6 and 2.5 wt.% (Figure 6, blue and green lines) leads to a substantial

enhancement of the BiSI and $Bi_{13}S_{18}I_2$ reflections and the disappearance of the SiO_2 peaks, indicating complete surface coverage and improved crystallinity. At 2.5 wt.% PVP, the XRD pattern exhibits the highest overall peak intensity and improved peak definition for both BiSI and $Bi_{13}S_{18}I_2$ phases, indicating enhanced crystallinity and preferred orientation of the coexisting phases. The reflections at (020), (220), and (201) correspond to BiSI, while the (110) reflection is attributed to $Bi_{13}S_{18}I_2$. Further increase of the PVP amount to 3.0 wt.% (Figure 6, purple line) leads to a decrease in the intensities of the chalcohalide reflections and the appearance of weak Bi_2S_3 features, which can be attributed to increased solution viscosity and partial surface passivation by excess polymer, suppressing Bi-S-I crystallization. At 3.0 wt.% PVP, the XRD pattern exhibits a pronounced reduction in diffraction peak intensity and peak definition, indicating suppressed crystallinity of the deposited film. The presence of an amorphous phase cannot be unambiguously confirmed by XRD alone and is therefore not claimed. Rietveld refinement (Table S1, Supplementary material) confirms the qualitative trends of phase evolution. The refinement parameters (R_p, R_{wp}, R_{exp} and χ^2) are within the acceptable range for reliable Rietveld refinement. For the optimal composition (2.5 wt.% PVP), the $Bi_{13}S_{18}I_2$ and BiSI phases predominate with minimal SnO_2 remnants from the substrate. A decrease in PVP concentration leads to lower crystallinity, as evidenced by reduced diffraction peak intensity. While the absence of PVP yields a BiOI-dominant system (91.6 wt.%), accompanied by minor amounts of BiSI (6.5 wt.%) and $Bi_{13}S_{18}I_2$ (1.9 wt.%).

These results indicate that PVP plays a critical role in regulating the phase formation pathway of Bi-S-I compounds. The optimal concentration (2.5 wt.%) strikes a balance between precursor complex stabilization and controlled crystallite growth, yielding the highest structural order among the synthesized films. Thus, PVP acts not only as a steric stabilizer but also as a structure-modulating additive that influences nucleation pathways and qualitative phase evolution, rather than strictly controlling the relative phase fraction.

Photoelectrochemical characterization of BiSI/$Bi_{13}S_{18}I_2$ thin films

Figure 7 demonstrates the effect of PVP concentration in the precursor solution on the PEC characteristics of BiSI/$Bi_{13}S_{18}I_2$/FTO photoanodes synthesized *via* chemical bath deposition at 3.0, 2.5, 1.5 and 0.8 wt.% PVP. Measurements were carried out in 0.5 M Na_2SO_4 under modulated blue LED illumination (λ = 465 nm, 10 mW cm^{-2}) at a sweep rate of 5 mV s^{-1}. BiOI samples obtained in the absence of PVP were excluded from the PEC evaluation due to differences in phase composition.

All studied electrodes exhibit anodic photocurrent, confirming the n-type conductivity of the films. The photocurrent onset (≈ -100 mV) and dark current onset (≈ 650-700 mV) remain largely unaffected by PVP concentration, indicating that bulk band energetics remain unchanged while interfacial kinetics and charge-transport pathways are strongly morphology-dependent. The photocurrent density strongly depends on the PVP concentration: it increases from J_{ph} ≈ 0.27 μA cm^{-2} at 0.8 wt.% to a maximum of J_{ph} ≈ 15.7 μA cm^{-2} at 2.5 wt.% PVP, corresponding to nearly a 58-fold improvement. This enhancement is attributed to the formation of dense, uniform coatings that improve electrical connectivity between crystallites and the FTO layer, thereby minimizing grain-boundary recombination. At 3.0 wt.% PVP, the photocurrent decreases, consistent with SEM data showing the formation of large globular aggregates with an amorphous organic surface layer that limits conductive pathways.

Here, the quantum efficiency is expressed as the incident photon-to-current efficiency (IPCE), which is equivalent to the external quantum efficiency (EQE) and represents the ratio of collected charge carriers to incident photons at a given wavelength. In agreement with the photocurrent behaviour, the quantum efficiency (IPCE at 465 nm) also follows a non-monotonic trend (Figure 7b),

increasing from 0.04 ± 0.01 % (0.8 wt.% PVP) to 0.80 ± 0.02 % (1.6 wt.% PVP) and reaching a maximum of 2.62 ± 0.04 % (2.5 wt.% PVP), followed by a decrease to 1.82 ± 0.06 % (3.0 wt.% PVP) (Figure 7b). This correlation between photocurrent density and IPCE confirms that 2.5 wt.% PVP provides optimal microstructural conditions for efficient charge separation and interfacial charge transfer. The IPCE value obtained in this work (2.62% at 465 nm) is fully consistent with previously reported ranges for chalcohalide BiSI/$Bi_{13}S_{18}I_2$ systems in sulphate electrolytes and under short-wavelength illumination (typically 2-6%) [44].

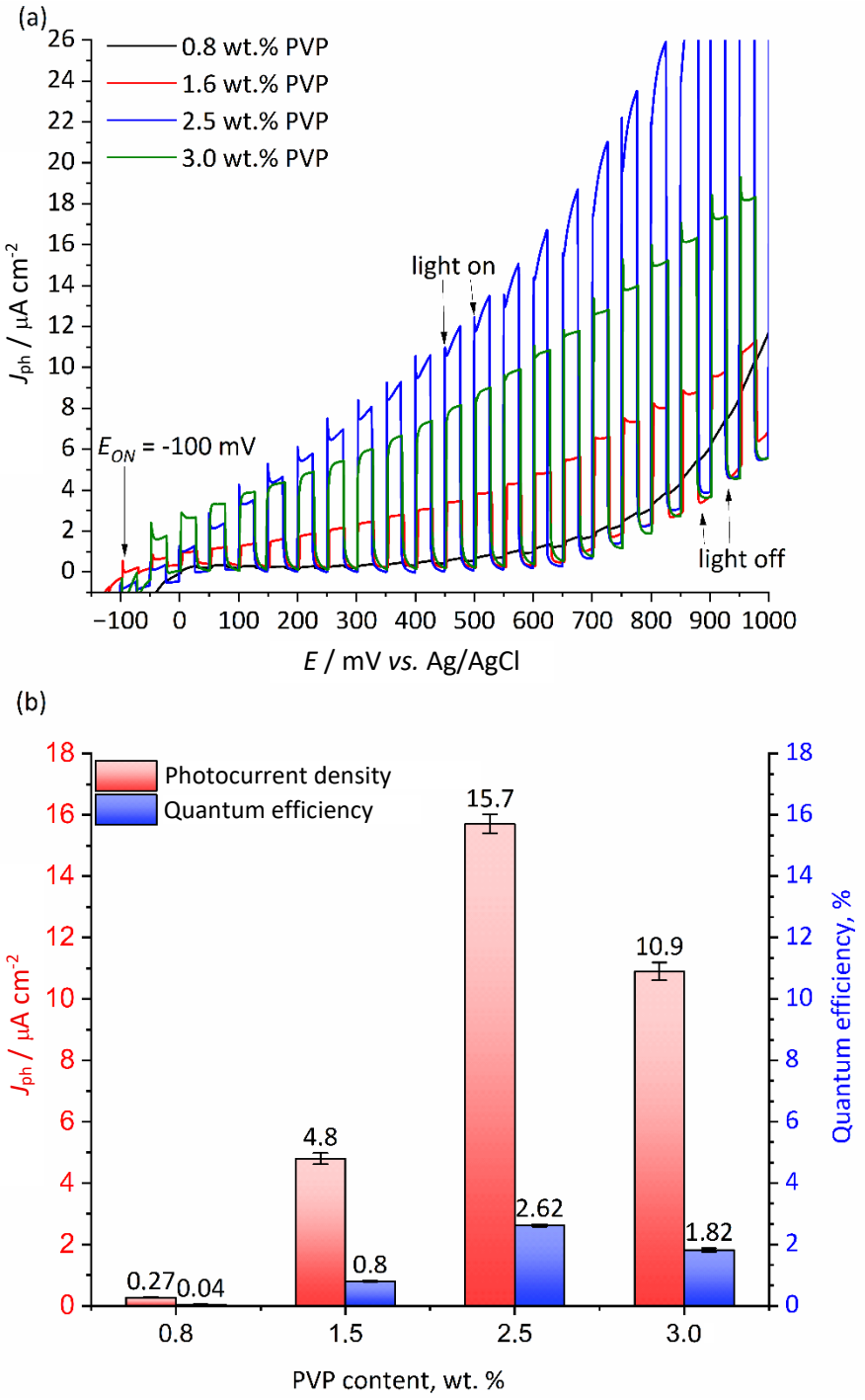

***Figure 7**. (a) Photocurrent density vs. electrode potential; (b) photocurrent density and quantum efficiency IPCE at 465 nm as a function of PVP concentration for BiSI/$Bi_{13}S_{18}I_2$/FTO thin films in 0.5 M Na_2SO_4 under blue LED illumination (λ = 465 nm, 10 mW cm^{-2})*

At potentials above ≈600 to 650 mV, a progressive increase in dark current is observed for all samples, which has also been reported for Bi- and Sb-containing chalcogenide photoanodes [61,62]. This phenomenon is associated with (i) activation of surface traps involved in electrochemical redox processes under high anodic bias, and (ii) the onset of photo-/electro-corrosion processes that proceed even in the absence of illumination, generating additional parasitic current.

A comprehensive comparison of PEC characteristics obtained in this study with literature data for BiSI, Bi_2S_3, BiOI and BiSI/$Bi_{13}S_{18}I_2$ in Na_2SO_4 (including exact IPCE values), as well as for measurements performed in sulphide/iodide electrolytes (Na_2S, Na_2S + S, KI, I^-/I_3^-), for complex heterostructures/composites, and under AM1.5G *vs.* blue-LED illumination is summarized in Table S2. Table S2 shows that although the IPCE values reported here are lower than some reported in the literature, they were obtained under more conservative, comparable conditions. The measurements were carried out for single thin films in a neutral Na_2SO_4 electrolyte, without sacrificial agents, co-catalysts, or complex heterostructures. As a result, the data reflect the intrinsic PEC performance of the BiSI/$Bi_{13}S_{18}I_2$ system and can serve as a realistic reference for further material optimization.

Photoelectrochemical behaviour in electrolytes with different redox activity

To decouple intrinsic semiconductor properties from electrolyte-induced interfacial effects, PEC measurements were also performed in electrolytes with varying redox activity. The PEC behaviour of BiSI/$Bi_{13}S_{18}I_2$ thin film photoanodes was evaluated in three aqueous electrolytes with different redox characteristics:

1) 0.5 M Na_2SO_4 (electrochemically inert medium);

2) 0.1 M Na_2SO_3 (sacrificial hole scavenger);

3) a mixed electrolyte of 0.1 M Na_2SO_3 + 0.5 M Na_2SO_4.

All measurements were performed under chopped blue-light illumination (λ = 465 nm, 10 mW cm^{-2}). For comparison, J_{ph}-E characteristics were obtained for the BiSI/$Bi_{13}S_{18}I_2$ photoanode synthesized at 2.5 wt.% PVP, the composition previously identified as optimal in terms of morphology, phase purity and PEC response. This serves as a reference for analysing the effect of redox-active species in the electrolyte.

Figure 8a (black curve) shows the behaviour of the BiSI/$Bi_{13}S_{18}I_2$ photoanode in 0.5 M Na_2SO_4, which reflects the intrinsic PEC performance of the heterophase system. The dark current is negligible up to ~600 to 650 mV, while illumination induces a steadily increasing anodic photocurrent. The maximum photocurrent density is J_{ph} = 15.7 ± 0.31 μA cm^{-2}, with an IPCE at 465 nm of 2.62 ± 0.04 %. A minor rise in dark current above ~650 mV is consistent with the previously reported behaviour of Bi-based chalcogenides, in which surface states and anodic corrosion pathways become electrochemically active at elevated bias [20]. In 0.1 M Na_2SO_3 (Figure 8a, red curve), the PEC response changes markedly, a pronounced dark current is detected even without illumination, and the photocurrent increases in parallel without reaching a saturation region. This behaviour is attributed to the rapid oxidation of sulphite ions (SO_3^{2-}), which is both thermodynamically and kinetically more favourable than the oxidation of water. Thus, even thermally generated carriers or defect-mediated surface states can initiate faradaic SO_3^{2-} oxidation at positive potentials. The maximum photocurrent density and IPCE at 465 nm are J_{ph} = 3.11 ± 0.24 μA cm^{-2} and IPCE = 0.81 ± 0.09 %, respectively (Figure 8b). Although hole extraction is significantly accelerated, this regime is limited by parasitic dark reactions and rapid interfacial degradation, consistent with general observations of accelerated photocorrosion and dark faradaic reactions in metal sulphide photoanodes operating in sulphite-containing electrolytes [63,64]. The mixed electrolyte (Figure 8a, blue curve) combines features of both inert and

sacrificial systems. Efficient hole scavenging by SO_3^{2-} suppresses recombination and enhances interfacial charge transfer, resulting in the highest photocurrent density (J_{ph} = 25.21 ± 0.38 μA cm^{-2}) and IPCE at 465 nm = 6.67 ± 0.12 % (Figure 8b). At the same time, the noticeable increase in dark current at higher potentials indicates the onset of sulphite oxidation even in the dark and a reduction in charge-transfer resistance. This balance highlights that enhanced PEC activity is accompanied by increased susceptibility to long-term interfacial degradation.

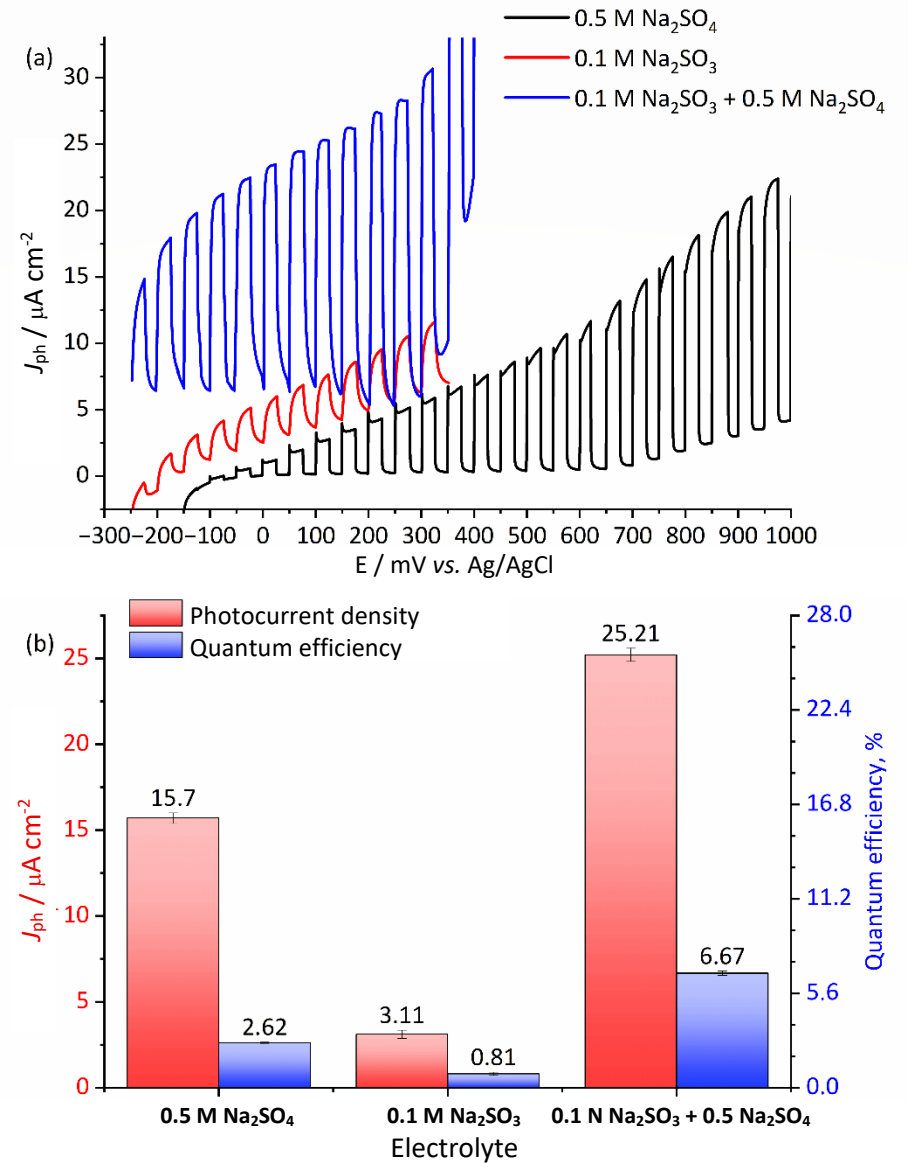

Figure 8. *(a) Photocurrent density-potential curves of BiSI/$Bi_{13}S_{18}I_2$/FTO photoanodes; (b) maximum photocurrent density and IPCE at 465 nm extracted from PEC and spectral measurements, recorded in electrolytes with different redox activity*

This interpretation is further supported by EIS analysis (Figure 9), which shows that the enhanced photocurrent in the mixed electrolyte does not correspond to the lowest interfacial charge-transfer resistance, highlighting the complex interplay between charge-transfer kinetics and interfacial stability. To further elucidate the origin of the electrolyte-dependent PEC behaviour, electrochemical impedance spectroscopy (EIS) was performed under illumination at 0.65 V *vs.* Ag/AgCl for 0.5 M Na_2SO_4 electrolyte and at 0 V *vs.* Ag/AgCl for 0.1 M Na_2SO_3 and Na_2SO_4/Na_2SO_3 electrolytes, selected to minimize excessive dark currents in sulphite-containing media. Figure 9 presents the Nyquist plots of BiSI/$Bi_{13}S_{18}I_2$/FTO photoanodes recorded in different electrolytes.

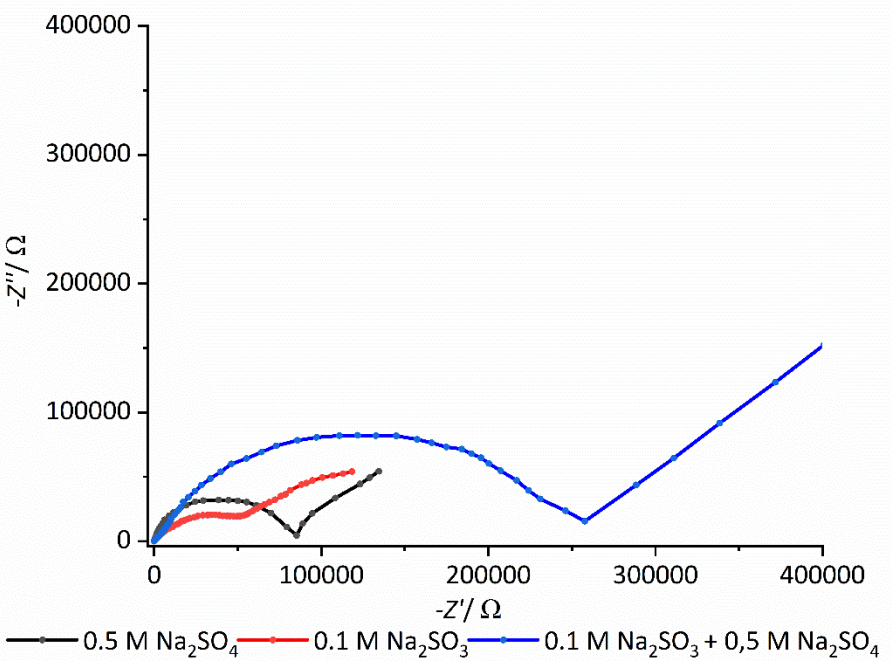

Figure 9. *Nyquist plots of BiSI/$Bi_{13}S_{18}I_2$/FTO photoanodes recorded under illumination in different electrolytes: 0.5 M Na_2SO_4, 0.1 M Na_2SO_3, and mixed Na_2SO_4/Na_2SO_3*

At higher frequencies, impedance spectra consist of a single non-ideal semicircle that was analysed using an equivalent circuit comprising the solution resistance (R_s) in series with a parallel combination of charge-transfer resistance (R_{ct}) and a constant phase element (CPE), accounting for non-ideal interfacial capacitive behaviour of the polycrystalline heterophase films. The corresponding equivalent-circuit fitting parameters obtained from EIS analysis are summarized in Table S3 (Supporting Information), enabling a direct comparison of interfacial charge-transfer characteristics across the investigated electrolytes. The smallest semicircle diameter, corresponding to the lowest R_{ct}, is observed in 0.1 M Na_2SO_3, reflecting highly efficient hole extraction via sulphite oxidation. In contrast, a larger R_{ct} is obtained in the inert 0.5 M Na_2SO_4 electrolyte, indicating sluggish interfacial charge-transfer kinetics associated with water oxidation. Interestingly, the mixed Na_2SO_4/Na_2SO_3 electrolyte exhibits higher R_{ct} compared to pure Na_2SO_3, which can be attributed to more complex interfacial processes, including competitive adsorption of sulphate and sulphite species and modification of the electrical double layer. These EIS results demonstrate that the highest photocurrent and IPCE observed in the mixed electrolyte arise from enhanced hole scavenging rather than from intrinsically lower interfacial resistance. Thus, EIS provides direct evidence that interfacial charge-transfer kinetics, rather than bulk light absorption, represent the primary limiting factor in the studied BiSI/$Bi_{13}S_{18}I_2$ photoanodes.

Although the IPCE value obtained for the BiSI/$Bi_{13}S_{18}I_2$ photoanodes in this work (2.62 ± 0.04 % at 465 nm in 0.5 M Na_2SO_4) is lower than the highest values reported in the literature (Table S2), this difference can be rationalized by fundamental distinctions in film morphology, crystallinity, and experimental conditions. High IPCE values of 55-64 % have been reported for BiSI electrodes with needle-like or single-crystalline architectures, where the absence of intergranular barriers enables efficient separation of photogenerated electron-hole pairs within the space-charge region and promotes drift-diffusion transport of minority carriers toward the semiconductor/electrolyte interface. In contrast, the BiSI/$Bi_{13}S_{18}I_2$ films obtained in the present study exhibit a globular, polycrystalline morphology with a heterophase composition, which introduces grain boundaries and phase interfaces that act as additional recombination pathways, thereby limiting the external quantum efficiency.

Moreover, many literature reports achieving high IPCE values employ non-aqueous electrolytes, sacrificial hole scavengers (*e.g*. sulphide or iodide species), longer excitation wavelengths, or higher applied anodic bias, all of which significantly enhance apparent quantum efficiency by accelerating interfacial charge-transfer kinetics. In the present work, IPCE measurements were deliberately performed under conservative and technologically relevant aqueous conditions (0.5 M Na_2SO_4, λ = 465 nm), aiming to evaluate the intrinsic photoelectrochemical behaviour of BiSI-based photoanodes under regenerative PEC operation. The observed increase in IPCE to 6.67 ± 0.12 % upon addition of sulphite species confirms that interfacial hole-transfer kinetics, rather than optical absorption, constitute the primary limiting factor in the studied system. These results highlight the inherent trade-off between scalable thin-film fabrication, structural robustness, and maximum quantum efficiency in BiSI-based photoelectrodes.

Transient photocurrent responses recorded at a fixed potential (Figure S2a) further illustrate the effect of electrolyte composition. In 0.5 M Na_2SO_4, the photocurrent rapidly reaches a stable plateau, indicating low photocorrosion and a stable BiSI/$Bi_{13}S_{18}I_2$/electrolyte interface. In contrast, measurements performed in 0.1 M Na_2SO_3 exhibit a pronounced initial photocurrent spike followed by rapid decay, reflecting rapid hole extraction by sulphite ions and accelerated interfacial degradation driven by the aggressive anodic oxidation of sulphite. The mixed electrolyte combines features of both regimes: an enhanced initial photocurrent due to efficient hole scavenging by SO_3^{2-}, followed by a gradual attenuation under sustained anodic polarization, indicating improved charge-transfer kinetics at the expense of long-term interfacial stability.

Long-term photocurrent stability tests conducted under continuous illumination for 7200 s (Figure S2b) confirm these trends. In the 0.5 M Na_2SO_4 electrolyte, the photocurrent stabilizes at approximately J_{ph} = 10-12 μA cm^{-2}, indicating moderate but stable operation. In the sulfide-containing electrolyte (0.1 M Na_2SO_3), the photocurrent density rapidly decays to values below J_{ph} = 2 μA cm^{-2}, indicating severe interfacial degradation. The mixed electrolyte maintains a significantly higher steady-state photocurrent density of approximately J_{ph} = 18-20 μA cm^{-2}, highlighting the beneficial role of sulphite ions in enhancing charge transfer while simultaneously accelerating long-term degradation processes. The lower steady-state photocurrent observed during long-term operation, compared with transient measurements, is attributed to progressive surface oxidation, partial loss of active sites, and accumulation of interfacial defects under sustained anodic polarization, which are not captured in short-time transient experiments.

Thus, the observed trends demonstrate that Na_2SO_4 provides a benchmark for intrinsic PEC behaviour under oxygen evolution and ensures the best stability. Na_2SO_3 highlights defect-mediated pathways and interfacial instability, driven by rapid hole scavenging and strong parasitic dark reactions. Na_2SO_3 + Na_2SO_4 yields the highest photocurrent and IPCE but also reveals the vulnerability of BiSI/$Bi_{13}S_{18}I_2$ to corrosion in redox-active environments. Together, these findings provide a comprehensive assessment of charge-transfer behaviour and stability limits for Bi-based chalcogenide photoanodes and help define suitable operating conditions for PEC systems.

Conclusions

In this work, the effect of PVP concentration in the precursor solution on the morphology, phase composition, and photoelectrochemical response of BiSI/$Bi_{13}S_{18}I_2$ thin films obtained by chemical bath deposition was systematically investigated. The results demonstrate that polymer-assisted growth plays a decisive role in governing film continuity, crystallinity, and the relative formation of BiSI and $Bi_{13}S_{18}I_2$ phases.

An optimal PVP concentration of 2.5 wt.% yields compact, homogeneous films with complete substrate coverage and the highest photoelectrochemical performance, achieving a photo-current density of J_{ph} = 15.7 μA cm^{-2} and an IPCE of 2.62 % at 465 nm. Both lower (≤1.6 wt.%) and higher (3.0 wt.%) PVP contents result in discontinuous or passivated morphologies, reduced crystallinity, and markedly diminished PEC activity. In the absence of PVP, uncontrolled anisotropic growth gives rise to BiOI-rich hierarchical structures accompanied by a pronounced loss of photoactivity.

PEC measurements performed in electrolytes with different redox activity further elucidate the interplay between intrinsic semiconductor properties, interfacial charge-transfer kinetics, and electrochemical stability. While Na_2SO_4 reflects the intrinsic behaviour of the BiSI/$Bi_{13}S_{18}I_2$ photo-anodes and ensures the highest operational stability, sulphite-containing and mixed electrolytes promote enhanced hole-transfer rates but simultaneously induce increased dark currents and a higher susceptibility to anodic degradation.

Electrochemical impedance spectroscopy confirms that the enhancement of PEC performance in sulphite-containing electrolytes originates from accelerated interfacial hole-transfer kinetics, whereas the increased charge-transfer resistance observed in mixed electrolytes reflects the complexity of competing interfacial processes rather than intrinsically improved charge transport.

Overall, this study demonstrates that controlled polymer addition represents an effective strategy for tuning the structural and functional properties of Bi-based chalcohalide photoanodes. The established correlations between PVP concentration, microstructure, and photoelectron-chemical behaviour provide practical guidelines for optimizing BiSI/$Bi_{13}S_{18}I_2$ thin films and related ternary chalcogenide systems for solar-driven photoelectrochemical applications.

Supplementary material

Additional data are available at https://pub.iapchem.org/ojs/index.php/JESE/article/view/3153, or from the corresponding author on request.

Conflict of Interest: *The authors declare no competing interests.*

Acknowledgements: *The authors acknowledge the Laboratory of Physical Research Methods of the D.V. Sokolsky Institute of Fuel, Catalysis and Electrochemistry for providing access to SEM, EDS, and XRD facilities used for the structural and morphological characterization of the synthesized semiconductor thin films.*

Funding: *The authors received no financial support for the research, authorship, and/or publication of this article.*

Data Availability: *All data supporting the findings of this study are included in the published article and/or in the Supplementary Material.*

References

[1] B. Cai, M.V. Pavliuk, G. Berggren, F.M. Ho, R. Essakhi, S. Svetlund, H. Chen, B. König, Bio-hybrid photoelectrochemical catalysis for solar fuels and chemicals conversion, *Nature Communications* **16** (2025) 9131. https://dx.doi.org/10.1038/s41467-025-64931-9

[2] C. Jin, M. Han, Y. Wu, S. Wang, Solar-driven photoelectrochemical conversion of biomass: recent progress, mechanistic insights and potential scalability, *Energy & Environmental Science* **17** (2024) 7459-7511. https://dx.doi.org/10.1039/D4EE02332C

[3] R. Abdullah, A. A. Jalil, M. Asmadi, N. S. Hassan, M. B. Bahari, M. Alhassan, N. M. Izzudin, M. H. Sawal, R. Saravanan, H. Karimi-Maleh, Recent advances in zinc oxide-based photoanodes for photoelectrochemical water splitting, *International Journal of Hydrogen Energy* **107** (2024) 183-207. https://dx.doi.org/10.1016/j.ijhydene.2024.05.461

[4] Z. Kerrami, A. Sibari, O. Mounkachi, A. Benyoussef, M. Benaissa, Improved photo-electrochemical properties of strained SnO_2, *International Journal of Hydrogen Energy* **45** (2020) 11035-11039. https://dx.doi.org/10.1016/j.ijhydene.2018.03.199
[5] M.A.S. Alothoum, A review of the synthesis, structural, and optical properties of TiO_2 nanoparticles: Current state of the art and potential applications, *Crystals* **15** (2025) 944. https://dx.doi.org/10.3390/cryst15110944
[6] H. Lu, S. Song, Q. Jia, G. Liu, L. Jiang, Advances in Cu_2O-based photocathodes for photoelectrochemical water splitting, *Acta Physico-Chimica Sinica* **40** (2024) 2304035. https://dx.doi.org/10.3866/PKU.WHXB202304035
[7] P. Garg, L. Mohapatra, A.K. Poonia, A.K. Kushwaha, K.N.V.D. Adarsh, U. Deshpande, Single crystalline α-Fe_2O_3 nanosheets with improved photoelectrochemical performance for water splitting, *ACS Omega* **8** (2023) 38607-38618. https://dx.doi.org/10.1021/acsomega.3c05726
[8] B.D. Nguyen, I.-H. Choi, J.-Y. Kim, Strategies for enhancing $BiVO_4$ photoanodes for photoelectrochemical water splitting: A state-of-the-art review, *Nanomaterials* **15** (2025) 1494. https://dx.doi.org/10.3390/nano15191494
[9] Y. Bai, H. Bai, K. Qu, W. Shi, In situ approach to fabricate BiOI photocathode with oxygen vacancies: Understanding the N_2-reduced behavior in photoelectrochemical systems, *Chemical Engineering Journal* **362** (2019) 1026-1034. https://dx.doi.org/10.1016/j.cej.2019.01.051
[10] A.K. Salih, Q. Drmosh, M. Qamar, Z.H. Yamani, Tuning structural properties of WO_3 thin films for photoelectrocatalytic water oxidation, *Catalysts* **11** (2021) 381. https://dx.doi.org/10.3390/catal11030381
[11] W. Yang, J. Moon, Recent advances in earth-abundant photocathodes for photoelectrochemical water splitting, *ChemSusChem* **12** (2019) 1889-1899. https://dx.doi.org/10.1002/cssc.201801554
[12] P.N. Rudd, J. Huang, Metal ions in halide perovskite materials and devices, *Trends in Chemistry* **1** (2019) 394-409. https://dx.doi.org/10.1016/j.trechm.2019.04.010
[13] G. Schileo, G. Grancini, Lead or no lead? Availability, toxicity, sustainability and environmental impact of lead-free perovskite solar cells, *Journal of Materials Chemistry C* **9** (2021) 67-76. https://dx.doi.org/10.1039/D0TC04552G
[14] A.M. Ganose, C.N. Savory, D.O. Scanlon, Beyond methylammonium lead iodide: prospects for the emergent field of ns^2-containing solar absorbers, *Chemical Communications* **53** (2017) 20-44. https://dx.doi.org/10.1039/C6CC06475B
[15] N. Wang, H. Luo, L. Lu, P. Wu, G. Kang, J. Chen, T. Xia, H. Zhou, S. Zhang, One-step calcination decomposition synthesis of $Bi_5O_7NO_3$/β-Bi_2O_3 for efficient degradation of norfloxacin: Performance, mechanism and toxicity insights, *Chemical Engineering Journal* **524** (2025) 169507. https://dx.doi.org/10.1016/j.cej.2025.169507
[16] D. Tiwari, F. Cardoso-Delgado, D. Alibhai, M. Mombrú, D.J. Fermín, Photovoltaic performance of phase-pure orthorhombic BiSI thin films, *ACS Applied Energy Materials* **2** (2019) 3878-3885. https://dx.doi.org/10.1021/acsaem.9b00544
[17] X. Meng, Z. Zhang, Bismuth-based photocatalytic semiconductors: Introduction, challenges and possible approaches, *Journal of Molecular Catalysis A: Chemical 423* (2016) 533-549. http://dx.doi.org/10.1016/j.molcata.2016.07.030
[18] K. Adams, A.F. Gonzalez, J. Mallows, T. Li, J.H.J. Thijssen, N. Robertson, Facile synthesis and characterization of $Bi_{13}S_{18}I_2$ films as a stable supercapacitor electrode material, *Journal of Materials Chemistry A* **7** (2019) 1638-1646. https://dx.doi.org/10.1039/C8TA11029H
[19] M. Mombrú Frutos, C. Grosso, Á. Olivera, H. Bentos Pereira, L. Fornaro, I. Aguiar, Understanding the crystal growth of bismuth chalcohalide nanorods through a self-

sacrificing template process: A comprehensive study, *Inorganic Chemistry* **61** (2022) 9231-9241. https://dx.doi.org/10.1021/acs.inorgchem.2c00846

[20] S. Li, L. Xu, X. Kong, T. Kusunose, N. Tsurumachi, Q. Feng, Bismuth chalcogenide iodides of $Bi_{13}S_{18}I_2$ and BiSI: Solvothermal synthesis, photoelectric behavior, and photovoltaic performance, *Journal of Materials Chemistry C* **8** (2020) 3821-3829. https://dx.doi.org/10.1039/C9TC05139B

[21] N.T. Hahn, J.L. Self, C.B. Mullins, BiSI micro-rod thin films: Efficient solar absorber electrodes?, *Journal of Physical Chemistry Letters* **3** (2012) 1571-1576. https://dx.doi.org/10.1021/jz300515p

[22] H. Sun, X. Xiao, V. Celorrio, Z. Guo, Y. Hu, C. Kirk, N. Robertson, A novel method to synthesize BiSI uniformly coated with rGO by chemical bonding and its application as a supercapacitor electrode material, *Journal of Materials Chemistry A* **9** (2021) 15452-15461. https://dx.doi.org/10.1039/D1TA02988F

[23] Z.S. Aliev, S.S. Musayeva, F.Y. Jafarli, I.R. Amiraslanov, A.V. Shevelkov, M.B. Babanly, The phase equilibria in the Bi-S-I ternary system and thermodynamic properties of the BiSI and $Bi_{19}S_{27}I_3$ ternary compounds, *Journal of Alloys and Compounds* **610** (2014) 522-528. https://dx.doi.org/10.1016/j.jallcom.2014.05.015

[24] X.A. Leontyeva, M.B. Dergacheva, D.S. Puzikova, G.M. Khussurova, P.V. Panchenko, Synthesis and properties of semiconductor bismuth sulfide iodide for photoelectrochemical applications, *Journal of Saudi Chemical Society* **27** (2023) 101694. https://dx.doi.org/10.1016/j.jscs.2023.101694

[25] H. Shi, W. Ming, M.H. Du, Bismuth chalcohalides and oxyhalides as optoelectronic materials, *Physical Review B* **93** (2016) 104108. https://dx.doi.org/10.1103/PhysRevB.93.104108

[26] C. Zhou, R. Wang, C. Jiang, J. Chen, G. Wang, Dynamically optimized multi-interface novel BiSI-promoted redox sites spatially separated n-p-n double heterojunctions BiSI/MoS_2/CdS for hydrogen evolution, *Industrial & Engineering Chemistry Research* **58** (2019) 7844-7856. https://dx.doi.org/10.1021/acs.iecr.9b00234

[27] R. Zhang, Z. Chen, C. Zhao, L. Cai, J. Yu, Z. Yang, J. Jiang, Synthesis of BiSI/Ag_2CO_3 composite material for photocatalytic degradation of rhodamine B under visible light, *Chemistry Select* **7** (2022) e202201243. https://dx.doi.org/10.1002/slct.202201243

[28] S. Farooq, T. Feeney, J. Mendes, V. Krishnamurthi, S. Walia, E. Gaspera, J. van Embden, High-gain solution-processed carbon-free BiSI chalcohalide thin film photodetectors, *Advanced Functional Materials* **31** (2021) 2109375. https://dx.doi.org/10.1002/adfm.202104788

[29] Y.C. Choi, E. Hwang, Controlled growth of BiSI nanorod-based films through a two-step solution process for solar cell applications, *Nanomaterials* **9** (2019) 1711. https://dx.doi.org/10.3390/nano9121650

[30] M.E. Kazyrevich, D.Y. Ivashenka, E.A. Bondarenko, E.A. Streltsov, A.I. Kulak, Synthesis and photoelectrochemical properties of bismuth thioiodide, *Proceedings of the National Academy of Sciences of Belarus Chemical Series* **54** (2018) 413-418 https://dx.doi.org/10.29235/1561-8331-2018-54-4-413-418

[31] M. Abbas, L. Zeng, F. Guo, M. Rauf, X.C. Yuan, B. Cai, A Critical Review on Crystal Growth Techniques for Scalable Deposition of Photovoltaic Perovskite Thin Films, *Materials* **13** (2020) 4851. https://dx.doi.org/10.3390/ma13214851

[32] A.P. Arun, N. Sreenivasan, J.H. Patil, R. Kusanur, H.L. Ramachandraiah, M. Ramakrishna, Thin Films for Next Generation Technologies: A Comprehensive Review of Fundamentals, Growth, Deposition Strategies, Applications, and Emerging Frontiers, *Processes* **13** (2025) 3846. https://dx.doi.org/10.3390/pr13123846

[33] S. Xu, D. Cao, Y. Liu, Y. Wang, Role of additives in crystal nucleation from solutions: A review, *Crystal Growth & Design* **22** (2022) 1175-1202. https://dx.doi.org/10.1021/acs.cgd.1c00776

[34] H. Cheng, L. Mao, S. Zhang, H. Lv, Impacts of polymeric additives on nucleation and crystal growth of indomethacin from supersaturated solutions, *AAPS PharmSciTech* **20** (2019) 193. https://dx.doi.org/10.1208/s12249-019-1387-y

[35] L. Chen, B. Guan, J. Guo, Y. Chen, Z. Ma, J. Chen, S. Yao, C. Zhu, H. Dang, K. Shu, Z. Guo, C. Yi, K. Shi, Y. Li, J. Hua, Z. Huang, Review on the preparation and performance improvement methods of bismuth photocatalyst materials, *Catalysis Science & Technology* **13** (2023) 5478-5529. https://dx.doi.org/10.1039/D3CY00760J

[36] V. Mahmoodi, A. Ahmadpour, T. Rohani Bastami, M.T. Hamed Mousavian, Facile synthesis of BiOI nanoparticles at room temperature and evaluation of their photoactivity under sunlight irradiation, *Photochemistry and Photobiology* **94** (2018) 4-16. https://dx.doi.org/10.1111/php.12832

[37] K. Abitaev, P. Atanasova, J. Bill, N. Preisig, I. Kuzmenko, J. Ilavsky, Y. Liu, T. Sottmann, In situ ultra-small- and small-angle X-ray scattering study of ZnO nanoparticle formation and growth through chemical bath deposition in the presence of polyvinylpyrrolidone, *Nanomaterials* **13** (2023) 2180. https://dx.doi.org/10.3390/nano13152180

[38] K. Dashtian, S. Hajati, M. Ghaedi, M. Rashid, M. Zarghami Qaretapeh, M. Rahimi-Nasrabadi, A $Bi_{13}S_{18}I_2$-based wearable photoelectrochemical biosensor for accurate monitoring of L-tyrosine in sweat as a diabetes biomarker, *Journal of Materials Chemistry B* **13** (2025) 5832-5844. https://dx.doi.org/10.1039/D5TB00095

[39] Z. Altaf, M. Imran, A. Haider, I. Shahzadi, Z. Mateen, A. Ul-Hamid, A.M. Fouda, M. Ikram, Synergistic catalytic and antibacterial activity, along with in silico molecular docking of bimetallic silver-copper-doped PVP-$Mg(OH)_2$ nanostructures, *Nanoscale Advances* **7** (2025) 7028-7039. https://dx.doi.org/10.1039/D5NA00693G

[40] R. Dhir, Photocatalytic degradation of methyl orange dye under UV irradiation in the presence of synthesized PVP-capped pure and gadolinium-doped ZnO nanoparticles, *Chemical Physics Letters* **746** (2020) 137302. https://dx.doi.org/10.1016/j.cplett.2020.137302

[41] K.M. Koczkur, S. Mourdikoudis, L. Polavarapu, S.E. Skrabalak, Polyvinylpyrrolidone (PVP) in nanoparticle synthesis, *Dalton Transactions* **44** (2015) 17883-17905. https://dx.doi.org/10.1039/C5DT02964C

[42] T. Ding, J. Dai, J. Xu, J. Wang, W. Tian, K. Huo, Y. Fang, C. Chen , 3D hierarchical Bi_2S_3 nanostructures by polyvinylpyrrolidone (PVP) and chloride ion-assisted synthesis and their photodetecting properties, *Nanoscale Research Letters* **10** (2015) 286. https://dx.doi.org/10.1186/s11671-015-0993-1

[43] M.B. Dergacheva, X.A. Leontyeva, G.M. Khussurova, D.S. Puzikova, P.V. Panchenko, Chemical deposition of bismuth iodide sulfide semiconductor thin films, *Reports of National Academy of Science of the Republic of Kazakhstan* **5** (2021) 100-108. https://dx.doi.org/10.32014/2021.2518-1483.88

[44] X.A. Leontyeva, N.A. Ivanova, G.M. Khussurova, D.S. Puzikova, A.K. Galeyeva, Photoelectrochemical performance of BiSI/$Bi_{13}S_{18}I_2$ thin films prepared via one-step chemical bath deposition, *Electroanalysis* **37** (2025) e70079. https://dx.doi.org/10.1002/elan.70079

[45] I. Aguiar, M. Mombrú, M.E. Pérez Barthaburu, L. Fornaro, Influence of solvothermal synthesis conditions on BiSI nanostructures for application in ionizing radiation detectors, *Materials Research Express* **3** (2016) 025012. https://dx.doi.org/10.1088/2053-1591/3/2/025012

[46] K. Mistewicz, T.K. Das, B. Nowacki, A. Smalcerz, H.J. Kim, S. Hajra, M. Godzierz, O. Masiuchok, Bismuth sulfoiodide (BiSI) nanorods: synthesis, characterization, and photodetector application, *Scientific Reports* **13** (2023) 8800. https://dx.doi.org/10.1038/s41598-023-35899-7

[47] E.A. Bondarenko, A.I. Kulak, A.V. Mazanik, I.A. Svito, E.A. Streltsov, Photoelectrochemical BiSI-based visible light detector, *Optical Materials* **159** (2025) 116654. https://doi.org/10.1016/j.optmat.2025.116654
[48] N.T. Hahn, A.J.E. Rettie, S.K. Beal, R.R. Fullon, C.B. Mullins, n-BiSI thin films: Selenium doping and solar cell behavior, *The Journal of Physical Chemistry C* **116** (2012) 24878-24886. https://doi.org/10.1021/jp3088397
[49] V. Sugathan, B. Ghosh, P.C. Harikesh, V. Kotha, P. Vashishtha, T. Salim, A. Yella, N. Mathews, Synthesis of bismuth sulphoiodide thin films from single precursor solution, *Solar Energy* **230** (2021) 714-720. https://dx.doi.org/10.1016/j.solener.2021.10.041
[50] H. Kunioku, M. Higashi, R. Abe, Low-temperature synthesis of bismuth chalcohalides: candidate photovoltaic materials with continuously controllable band gap, *Scientific Reports* **6** (2016) 32664. https://dx.doi.org/10.1038/srep32664
[51] Q. Wang, Y. Hui, Photo-driven cycling electro-Fenton catalysis via the synergistic effect of dual cathodes for energy-efficient water decontamination: Insights into performance, reaction mechanism and toxicity, *Chemical Engineering Journal* **507** (2025) 160487. https://dx.doi.org/10.1016/j.cej.2025.160487
[52] X. Shi, L. Cai, M. Ma, X. Zheng, J.H. Park, General characterization methods for photoelectrochemical cells for solar water splitting, *ChemSusChem* **8** (2015) 3192-3203. https://dx.doi.org/10.1002/cssc.201500075
[53] M. Shahmiri, N.A. Ibrahim, F. Shayesteh, N. Motallebi, Preparation of PVP-coated copper oxide nanosheets as antibacterial and antifungal agents, *Journal of Materials Research* **28** (2013) 3029-3037. https://dx.doi.org/10.1557/jmr.2013.31
[54] R.M. Zahari, A.H. Shaari, Z. Abbas, H. Baqiah, S.K. Chen, K.P. Lim, M.M. Awang Kechik, Simple preparation and characterization of bismuth ferrite nanoparticles by thermal treatment method, *Journal of Materials Science: Materials in Electronics* **28** (2017) 17932-17938. https://dx.doi.org/10.1007/s10854-017-7735-3
[55] M. Li, R.K. Li, Two new bismuth thiourea bromides: Crystal structure, growth, and characterization, *Dalton Transactions* **43** (2014) 2577-2580. https://dx.doi.org/10.1039/C3DT52953C
[56] H. Sun, G. Yang, J. Chen, C. Kirk, N. Robertson, Facile synthesis of BiSI and $Bi_{13}S_{18}I_2$ as stable electrode materials for supercapacitor applications, *Journal of Materials Chemistry C* **8** (2020) 13253-13262. https://dx.doi.org/10.1039/D0TC02993A
[57] M.G. Naseri, E.B. Saion, H.A. Ahangar, M. Hashim, A.H. Shaari, Simple preparation and characterization of nickel ferrite nanocrystals by a thermal treatment method, *Powder Technology* **212** (2011) 80-88. https://dx.doi.org/10.1016/j.powtec.2011.04.033
[58] A. Abedini, E. Saion, F. Larki, A. Zakaria, M. Noroozi, N. Soltani, Room temperature radiolytic synthesized Cu@$CuAlO_2$-Al_2O_3 nanoparticles, *International Journal of Molecular Sciences* **13** (2012) 11941-11953. https://dx.doi.org/10.3390/ijms130911941
[59] W. Dai, Y. Zhang, P. Deng, W. Zhang, S. He, Y. Gou, X. Xie, K. Zhang, J. Li, L. Lin, X. Wang, Enhancing stability and efficiency of perovskite solar cells via polymer-additive crystallization, *Nano Energy* **58** (2019) 234-243. https://dx.doi.org/10.1021/acsami.4c14573
[60] N.A. Abdul-Manaf, A.H. Azmi, F. Fauzi, N.S. Mohamed, The effects of micro and macro structure on electronic properties of bismuth oxyiodide thin films, *Materials Research Express* **8** (2021) 096401. https://dx.doi.org/10.1088/2053-1591/ac20f7
[61] E.Ö. Alagöz, H. Jahangiri, S. Kaya, Profound influence of surface trap states on the utilization of charge carriers in CdS photoanodes, *Materials Advances* **5** (2024) 1513-1522. https://dx.doi.org/10.1039/D3MA00847A

[62] T.R. Harris-Lee, F. Marken, C.L. Bentley, J. Zhang, A.L. Johnson, A chemist's guide to photoelectrode development for water splitting - the importance of molecular precursor design, *EES Catalysis* **1** (2023) 832-873. https://dx.doi.org/10.1039/D3EY00176H
[63] J. A. Nasir, Z. U. Rehman, S. N. A. Shah, A. Khan, I. S. Butler, C. R. A. Catlow, Recent developments and perspectives in CdS-based photocatalysts for water splitting, *Journal of Materials Chemistry A* **8** (2020) 20752-20780 https://dx.doi.org/10.1039/D0TA05834C
[64] L. Meng, L. Li, Recent research progress on operational stability of metal oxide/sulfide photoanodes in photoelectrochemical cells, *Nano Research Energy* **1** (2022) 9120020. https://dx.doi.org/10.26599/NRE.2022.9120020